

# First-Principles Study of Substitutional Metal Impurities in Graphene: Structural, Electronic and Magnetic Properties

E. J. G. Santos,<sup>\*</sup> A. Ayuela,<sup>†</sup> and D. Sánchez-Portal<sup>‡</sup>

*Centro de Física de Materiales CFM-MPC, Centro Mixto CSIC-UPV/EHU, Apdo. 1072, 20080 San Sebastián, Spain and Donostia International Physics Center (DIPC), Paseo Manuel de Lardizabal 4, 20018 San Sebastián, Spain*

(Dated: February 13, 2022)

We present a theoretical study using density functional calculations of the structural, electronic and magnetic properties of 3d transition metal, noble metal and Zn atoms interacting with carbon monovacancies in graphene. We pay special attention to the electronic and magnetic properties of these substitutional impurities and found that they can be fully understood using a simple model based on the hybridization between the states of the metal atom, particularly the  $d$  shell, and the defect levels associated with an unreconstructed  $D_{3h}$  carbon vacancy. We identify three different regimes associated with the occupation of different carbon-metal hybridized electronic levels: (i) bonding states are completely filled for Sc and Ti, and these impurities are non-magnetic; (ii) the non-bonding  $d$  shell is partially occupied for V, Cr and Mn and, correspondingly, these impurities present large and localized spin moments; (iii) antibonding states with increasing carbon character are progressively filled for Co, Ni, the noble metals and Zn. The spin moments of these impurities oscillate between 0 and  $1 \mu_B$  and are increasingly delocalized. The substitutional Zn suffers a Jahn-Teller-like distortion from the  $C_{3v}$  symmetry and, as a consequence, has a zero spin moment. Fe occupies a distinct position at the border between regimes (ii) and (iii) and shows a more complex behavior: while is non-magnetic at the level of GGA calculations, its spin moment can be switched on using GGA+U calculations with moderate values of the U parameter.

PACS numbers: 73.22.-f, 73.20.Hb, 75.20.Hr, 61.48.De

## I. INTRODUCTION

The electronic properties of two-dimensional graphene are currently the subject of intense experimental and theoretical research.<sup>1,2</sup> Graphene exhibits many intriguing phenomena stemming from the characteristic conical dispersion and chiral behavior of its valence and conduction bands nearby the Fermi energy.<sup>3,4,5</sup> In general, graphenic nanostructures like graphene nanoribbons, carbon nanotubes and their interconnections, are opening new routes for research in the field of nanoelectronics<sup>6</sup>, due to the long spin relaxation and decoherence times of these materials<sup>7</sup>. In addition, the possibility to control the magnetism of edge states in nanoribbons by applying external electric fields,<sup>8,9</sup> make them very attractive for spintronic applications.<sup>10</sup> However, for the design of realistic devices the effect of defects and impurities have to be taken into account. For this reason, quite a lot of work has been devoted to the study of defects and different types of impurities in these materials. It has now become clear that defects and dopants severely affect some the properties of graphenic systems and can be used to tune their response. For example, the strong interplay between the presence of defect or dopants and the magnetic properties of carbon nanostructures has been stressed by several authors.<sup>11,12,13,14,15,16,17,18,19</sup>

Here we focus on substitutional impurities in graphene, in which a single metal atom substitutes one or several carbon atoms in the layer. Direct experimental evidence of the existence of these kind of defects has been recently provided by Gan *et al.*<sup>20</sup>. Using high-resolution transmission electron microscopy (HRTEM), these authors were

able to visualize individual Au and Pt atoms incorporated into a very thin graphitic layer probably consisting of one or two graphene layers. From the real-time evolution and temperature dependence of the dynamics they obtained information about the diffusion of these atoms. Large diffusion barriers ( $\sim 2.5$  eV) were observed for in-plane migration, which indicates the large stability of these defects and the presence of strong carbon-metal bonds. These observations seem to indicate that the atoms occupy substitutional positions. There also exists evidence for the existence of substitutional Ni impurities in single-walled carbon nanotubes (SWCNT)<sup>21,22</sup> and graphitic particles.<sup>23</sup> Ushiro *et al.*<sup>21</sup> showed that Ni substitutional defects were present in SWCNT samples even after careful purification and that, according to their analysis of the X-ray absorption data, the most likely configuration was one in which the Ni atom replaces a carbon atom, as seen in Fig. 1.

The presence of substitutional defects can have important implications for the interpretation of some experimental evidence. For example, substitutionals of magnetic transition metals are expected to strongly influence the magnetic properties of graphenic nanostructures. Interestingly transition metals, like Fe, Ni or Co, are among the most common catalysts used for the production of SWCNT<sup>24</sup>. Furthermore, Rodríguez-Manzo and Banhart<sup>25</sup> have recently demonstrated the possibility to create individual vacancies at desired locations in carbon nanotubes using electron beams. This ability, in combination with the observed stability of substitutional impurities, can open a route to fabricate new devices incorporating substitutional impurities in certain locations or arranged in particular ways. Such devices would al-

low for experimental verification of some of the unusual magnetic interactions mediated by the graphenic carbon network that have been predicted recently.<sup>26,27,28</sup>

In this work we study theoretically the structural, electronic and magnetic properties of  $3d$  transition metals, noble metals and Zn as substitutional impurities in graphene using density functional (DFT) calculations. We only consider the configuration proposed by Ushiro *et al.*,<sup>21</sup> in which a single metal atom binds to a carbon monovacancy. Throughout the paper we will refer to this structure as substitutional configuration. The results of our DFT calculations are in good agreement with the results of other recent studies on similar systems.<sup>22,28,29,30,31,32</sup> In particular, Krasheninnikov *et al.*<sup>29</sup> have presented the most complete first-principles study to date of metal atoms interacting with single and double vacancies in graphene. In most cases our results are in good agreement with their predictions and similar general trends are found. However, the electronic structure of these defects has not been analyzed in detail to date and no simple model to understand the observed behaviors has been presented so far. Here we present the evolution of the electronic structure of the substitutional defects as we move along the transition series and correlate the observed changes with a simple picture of the metal-vacancy interaction.

In our study we pay special attention to the electronic and magnetic properties of the metal impurities. One of our key results is that the electronic and magnetic properties of these substitutional metals can be fully understood using a simple model based on the hybridization between the states of the metal atom, particularly the  $d$  shell, and the defect levels associated with the unreconstructed carbon vacancy. The predictions of this model are in good agreement with the calculated DFT band structures. With this model we can easily understand the non-trivial behavior found for the binding energy and for the size and localization of the spin moment as we increase the number of valence electrons in the impurity. In brief, we have identified three different regimes that can be correlated with the electron filling of different carbon-metal hybridized levels: (i) bonding states are filled for Sc and Ti, and these impurities are non-magnetic; (ii) the non-bonding  $d$  shell is partially occupied for V, Cr and Mn and, correspondingly, these impurities present large and localized spin moments; (iii) antibonding states with increasing carbon character are progressively filled for Co, Ni, the noble metals and Zn, giving rise to spin moments that oscillate between 0 and  $1 \mu_B$  and are increasingly delocalized.

We have also found that Zn becomes non-magnetic due to a Jahn-Teller distortion. However, it is possible to stabilize a symmetric configuration with a spin moment of  $2\mu_B$  with a very small energy penalty of  $\sim 150$  meV. Finally, our calculations confirm that, the unexpected result that Au substitutionals<sup>29,30</sup> present a spin moment of  $1\mu_B$ , also holds for Ag and Cu, and thus stems only from the number of valence electrons (see the Slater-Pauling-

like plot in Fig. 3).

We have studied with special detail the complex case of Fe. This impurity occupies a distinct position at the boundary between two different regimes and its magnetic behavior stems from the competition between the carbon-metal hybridization and the electron-electron interaction within the  $3d$  shell. As a result, the spin moment of Fe is specially difficult to describe: although non-magnetic using standard functionals within the generalized gradient approximation (GGA)<sup>33</sup>, the magnetism of Fe appears using the so-called LDA+U methodology with reasonably low values of the U parameter.

The paper is organized as follows. After a brief description of the computational approach in Sec. II, we present a summary of the structure, energetics and magnetic properties of all the studied elements in Sec. III. In this section we also indicate the general ideas behind our model of the metal-carbon hybridization in these systems. In Sec. IV the electronic structure of the unreconstructed  $D_{3h}$  carbon vacancy in graphene is presented. This is one of the key ingredients to understand the binding and electronic structure of substitutional impurities in graphene. The electronic structure of the different groups of impurities is described in the subsequent sections, particularly in Sec. V. The Zn substitutional impurity with its Jahn-Teller distortions is described in Sec. VI. A special section (Sec. VII) is devoted to describe the special role of Fe at the border between two different regimes. Finally, we close with some general conclusions.

## II. THEORETICAL METHODS

We have used two different approaches to perform our DFT calculations: the SIESTA method<sup>34,35,36</sup> using a basis set of localized numerical-atomic-orbitals<sup>35,37</sup> (NAOs) and the VASP code<sup>38,39</sup> using a basis set of plane waves. We have used the Perdew-Burke-Ernzerhof<sup>33</sup> GGA (PBE-GGA) functional in all our calculations. Most of our results are obtained using a  $4\times 4$  supercell. This supercell is sufficiently large to obtain reliable results. This has been proven by performing calculations using larger supercells up to  $8\times 8$  for several elements. The utilized codes perform three-dimensional periodic calculations. In order to avoid spurious interactions between periodic images of the defective graphene layer, the size of the supercell perpendicular to the plane was always larger than  $15 \text{ \AA}$ . The convergence with respect to the number of  $k$ -points was specially critical to obtain accurate results for the spin moment in the studied systems. For all the impurities and different supercell sizes we have used a large number of  $k$ -points, consistent with a  $136\times 136$  Monkhorst-Pack<sup>40</sup> sampling of the unit cell of graphene, in combination with a Fermi-smearing of  $21 \text{ meV}$ . All the atomic coordinates were always optimized until forces along all directions were smaller than  $0.05 \text{ eV/\AA}$ .

For the SIESTA calculations we have used Troullier-

Martins norm-conserving pseudopotentials<sup>41</sup> generated using the pseudization radii shown in the Appendix. The pseudopotentials for the metal atoms include nonlinear core corrections<sup>42</sup> for exchange and correlation. The pseudocore radii ( $r_{core}$ ) have been optimized for each element and are also presented in the Appendix. Using nonlinear core corrections is known to be critical to describe properly the spin moment and magnetic properties of transition metals. We have tested that these pseudopotentials yield the correct spin moments and band structures in bulk phases.

The spacing of the real-space grid used to calculate the Hartree and exchange-correlation contribution to the total energy and Hamiltonian with SIESTA was equivalent to a 180 Ry plane-wave cutoff. A double- $\zeta$  polarized (DZP)<sup>35,37</sup> basis set has been used for the calculation of the magnetic and electronic properties. However, we have checked that using a double- $\zeta$  (DZ) basis set for carbon yields almost identical relaxed structures as the DZP basis and, therefore, we have used the smaller DZ basis for most of the structural relaxations. The shape of the basis orbitals was automatically determined by SIESTA using the algorithms described in Ref. 35. The cutoff radii of the different orbitals was obtained using an *energy shift* of 50 meV. Although this basis set proved to be sufficiently accurate to describe the geometries, spin moments and band structures, for some metal atoms the binding energies were slightly overestimated. For those atoms the radii of the basis orbitals were enlarged (using smaller values of the *energy shift* parameter) until binding energies were converged within a few tens of meV. The resulting radii are shown in the Appendix.

With the VASP code we have used a well converged plane-wave cutoff energy of 400 eV combined with the projected-augmented-wave (PAW) method. Using the provided PAW potentials allows to check the possible limitations of pseudopotential calculations. However, as shown below, the agreement between both sets of calculations is excellent. We have also performed GGA+U calculations using the formulation of Dudarev *et al.*<sup>43</sup>. In this formulation a single U parameter is used, which we have taken as an empirical parameter and varied in the range 1-4.5 eV in our calculations for all the studied impurities. Only for Fe, GGA+U results showed significant (qualitative) differences respect to those of PBE-GGA calculations.

### III. MAIN PROPERTIES OF SUBSTITUTIONAL TRANSITION METALS IN GRAPHENE

We provide in this section a brief summary of our results for the structure, binding, and spin moments of substitutional 3d transition metals, noble metals and Zn in graphene.

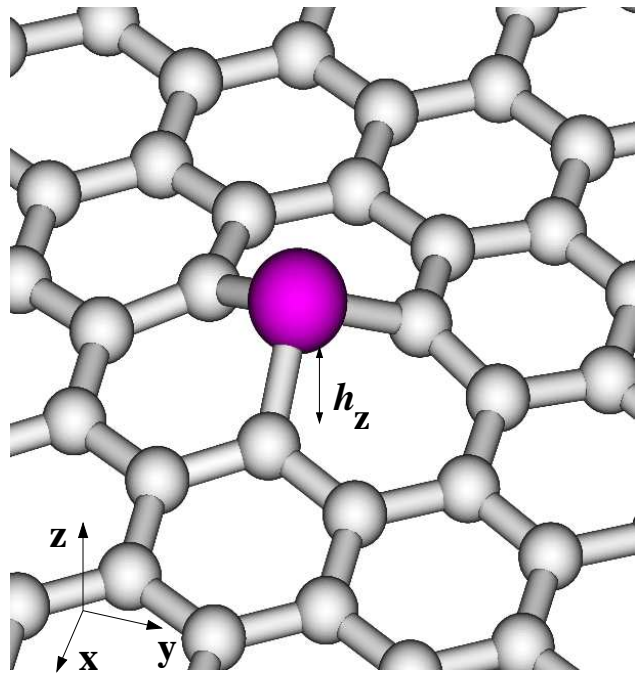


FIG. 1: (Color online) Typical geometry of transition and noble substitutional metal atoms in graphene. The metal atom moves upwards from the layer and occupies, in most cases, an almost perfectly symmetric three-fold position with  $C_{3v}$  symmetry.

#### A. Geometry and structural parameters

The typical geometry of the systems studied in this paper is presented in Fig. 1. The metal atom appears always displaced from the carbon layer. The height over the plane defined by its three nearest carbon neighbors is in the range 1.7-0.9 Å. These three carbon atoms are also displaced over the average position of the graphene layer by 0.3-0.5 Å. The total height ( $h_z$ ) of the metal atom over the graphene plane is the sum of these two contributions and ranges between 1.2-1.8 Å, as shown in panel (c) of Fig. 2. In most cases the metal atom occupies an almost perfect symmetric configuration with  $C_{3v}$  symmetry. Exceptions are the noble metals, that are slightly displaced from the central position, and Zn that suffers a Jahn-Teller distortion in its most stable configuration. However, we have found that it is also possible to stabilize a symmetric configuration for Zn with a binding energy only  $\sim 150$  meV smaller. This configuration was overlooked in a recently published study on these systems<sup>29</sup> and we will refer to it as  $Zn_{C_{3v}}$  throughout the paper.

Figures 2 presents a summary of the structural parameters of substitutional 3d transition metals, noble metals and Zn in graphene. Solid circles correspond to calculations using the SIESTA code with pseudopotentials and a basis set of atomic orbitals, while open squares stand for VASP calculations using plane-waves and PAW poten-

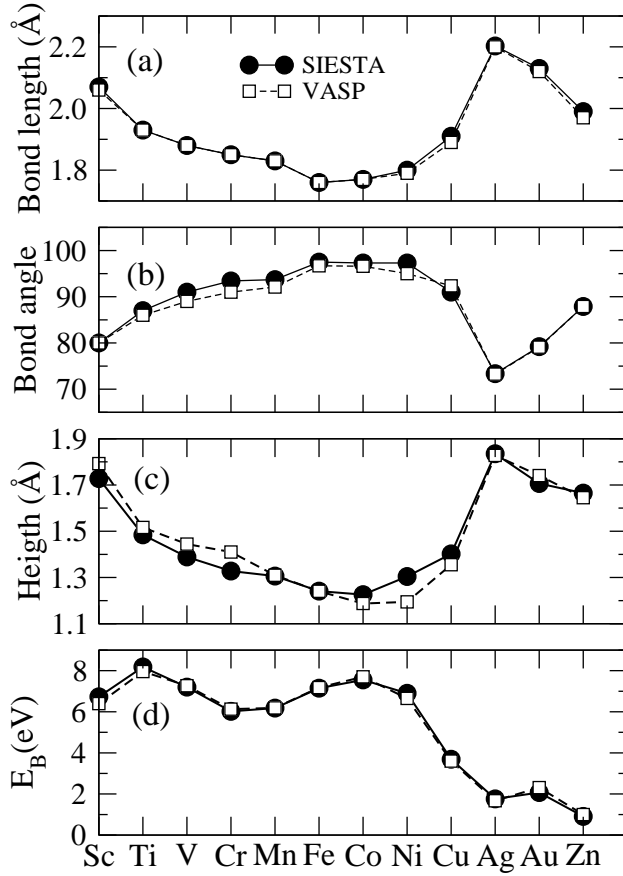


FIG. 2: Structural parameters and binding energies of substitutional transition and noble metals in graphene. Bond lengths and angles have been averaged for the noble metals. The data presented for Zn correspond to the high-spin solution with  $C_{3v}$  symmetry, and are very close to the averaged results for the most stable distorted solution.

tials. The agreement between both sets of calculations is quite remarkable. Data in these figures correspond to calculations using a  $4 \times 4$  supercell of graphene. For several metals we have also performed calculations using a larger  $8 \times 8$  supercell and find almost identical results. This is particularly true for the total spin moments, which are less dependent on the size of the supercell, but require a sufficiently dense k-point sampling to converge. In the following we will mainly discuss the results obtained with the smaller cell since the plots of the band structures are easier to interpret in that case. Finally, as already mentioned, noble metals and Zn present a distorted configuration. A detailed description of the structural parameters in these cases will be given below, here we only present the averaged structural data for noble metals and those corresponding to the  $Zn_{C_{3v}}$  case.

The data in Fig. 2 are basically consistent with those reported by Krashennnikov *et al.* in Ref. 29. The behavior of the metal-carbon bond length and the height ( $h_z$ ) of the impurity over the layer reflects approximately the size of the metal atom. For transition metals these dis-

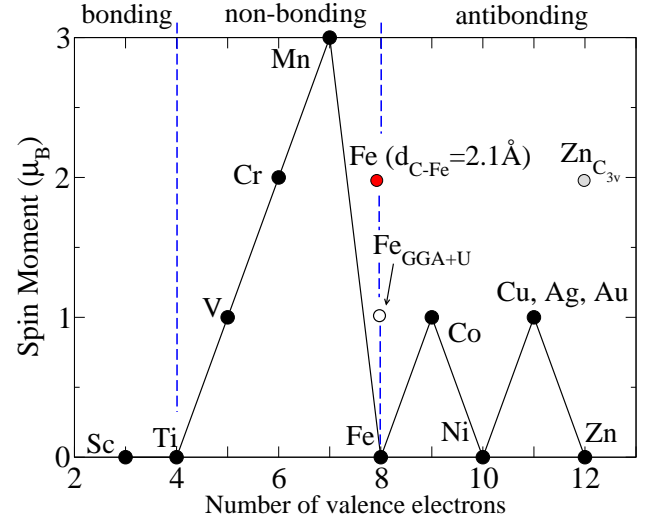


FIG. 3: (Color online) Spin moment of substitutional transition and noble metals in graphene as a function of the number of valence electrons (Slater-Pauling-type plot). Black symbols correspond to the most stable configurations using GGA. Results are almost identical using SIESTA and VASP codes. Three main regimes are found as explained in detail in the text: (i) filling of the metal-carbon bonding states gives rise to the non-magnetic behavior of Ti and Sc; (ii) non-bonding  $d$  states are filled for V, Cr and Mn giving rise to high spin moments; (iii) for Fe all non-bonding levels are occupied and metal-carbon antibonding states start to be filled giving rise to the observed oscillatory behavior for Co, Ni, Cu and Zn. Open and gray (red online) symbols correspond, respectively, to calculations of Fe using GGA+U and artificially increasing the height of the metal atom over the graphene layer (see the text). Symbol marked as  $Zn_{C_{3v}}$  corresponds to a Zn impurity in a high-spin symmetric  $C_{3v}$  configuration.

tances decrease as we increase the atomic number, with a small discontinuity when going from Mn to Fe. The carbon-metal bond length reaches its minimum for Fe ( $d_{C-Fe}=1.76$  Å), keeping a very similar value for Co and Ni. For Cu and Zn the distances increase reflecting the fully occupied  $3d$  shell and the large size of the  $4s$  orbitals. Among the noble metals we find that, as expected, the bond length largely increases for Ag with respect to Cu, but slightly decreases when going from Ag to Au. The latter behavior can be understood from the compression of the  $6s$  shell due to scalar relativistic effects.

## B. Binding energies

The binding energies of the studied substitutional metal atoms in graphene can be found in panel (d) of Fig. 2. In general, the behavior of the binding energies can be correlated with that of the carbon-metal bond length, although the former is somewhat more complicated. Binding energies for transition metals are in the range of 8-6 eV. Ti presents the maximum binding energy, which can be easily understood since for this ele-

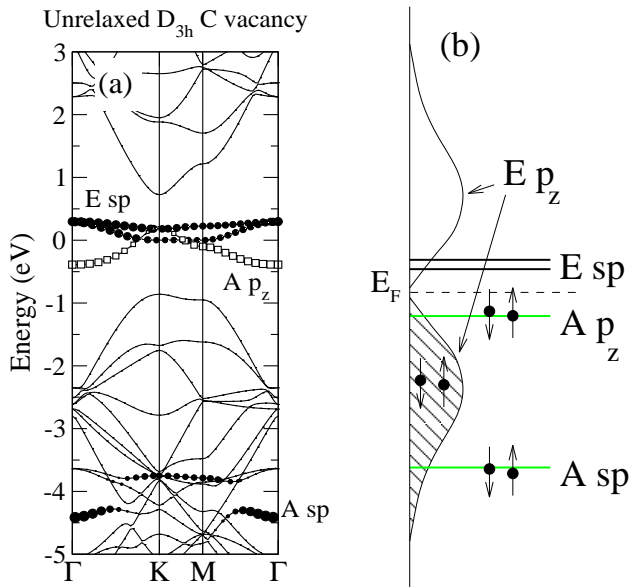


FIG. 4: (Color online) (a) Calculated band structure for an unrelaxed carbon vacancy ( $D_{3h}$  symmetry) in a  $4 \times 4$  supercell of graphene. Symbols indicated those bands with larger weight on the carbon atoms around the vacancy (solid symbols for bands with  $sp$  character and open symbols for a band with  $p_z$  character). The electronic structure near  $E_F$  is dominated by a fully symmetric  $p_z$  level ( $A p_z$ ) and two defect levels with  $E$  symmetry and  $sp$  character ( $E sp$ ). Notice that, due to the strong hybridization with the rest of the graphene layer, it is not possible to identify well defined defect levels with  $E$  symmetry and  $p_z$  character. (b) Scheme of the electronic structure of the  $D_{3h}$  C vacancy indicating the character and symmetry of the different levels and their occupations. Signal associated with the  $E p_z$  level extends over the whole valence and conduction band.

ment all the metal-carbon bonding states (see Sec. V A) become fully occupied. One could expect a continuous decrease of the binding energy as we move away from Ti along the transition metal series and first the non-bonding  $3d$  and later the metal-carbon antibonding levels become populated. However, the behavior is non-monotonic and the smaller binding energies among the  $3d$  transition metals are found for Cr and Mn, while a local maximum is observed for Co. This complex behavior is related to the simultaneous energy down-shift and compression of the  $3d$  shell of the metal as we increase the atomic number. This will become more transparent when discussing in detail the metal-carbon hybridization levels. In brief, the behavior of the binding energies of the substitutional  $3d$  transition metal comes from two competing effects:

(i) as the  $3d$  shell becomes occupied and moves to lower energies the hybridization with the carbon vacancy states near the Fermi energy ( $E_F$ ) is reduced, which decreases the binding energy;

(ii) the transition from Mn to late transition metals is accompanied by a shift of the metal-carbon bond length

of  $\sim 0.1$  Å, which increases the carbon-metal interaction and, correspondingly, the binding energy.

Binding energies for noble metals are considerably smaller than for transition metals and mirror the reverse behavior of the bond lengths: 3.69, 1.76 and 2.07 eV, respectively, for Cu, Ag and Au. The smallest binding energy ( $\sim 1$  eV) among the metals studied here is found for Zn, with filled  $s-d$  electronic shells.

### C. Spin moments

The spin moments of substitutional transition and noble metals in graphene are shown in Fig. 3. Again they are in agreement with the results of Ref. 29. However, we advance a simple model to understand the observed behavior which was not presented in that reference. One of the fundamental results of our study is a detailed model of the bonding and electronic structure of substitutional transition metals in graphene. As we will see below, the evolution of the spin moment can be completely understood using such model. In brief, we can distinguish different regimes according to the filling of electronic levels of different (bonding, non-bonding and antibonding) character:

(i) all the carbon-metal bonding levels are filled for Sc and Ti and, correspondingly, the spin-moment is zero;

(ii) non-bonding  $3d$  levels become populated for V and Cr giving rise to a spin moment of, respectively, 1 and  $2 \mu_B$  with a strong localized  $d$  character;

(iii) for Mn one additional electron is added to the antibonding  $d_{z^2}$  level and the spin moment increases to  $3 \mu_B$ ;

(iv) finally, for Fe and heavier atoms all the non-bonding  $3d$  levels are occupied and the spin moment oscillates between 0 and  $1 \mu_B$  as the antibonding metal-carbon levels become occupied.

The sudden decrease of the spin moment from  $3 \mu_B$  for Mn to  $0 \mu_B$  for Fe is characterized by a transition from a complete spin-polarization of the non-bonding  $3d$  levels to a full occupation of those bands. However, this effect depends on the ratio between the effective electron-electron interaction within the  $3d$  shell and the metal-carbon interaction (see Sec. VII). As we will see below, if the hybridization with the neighboring atoms is artificially reduced, for example by increasing the Fe-C distance, Fe impurities develop a spin moment of  $2 \mu_B$ . Our results also show that it is also possible to switch on the spin moment of Fe by changing the effective electron-electron interaction within the  $3d$  shell. This can be done using the so-called GGA+U method. For a large enough value of  $U$  (in the range 2-3 eV), Fe impurities develop a spin moment of  $1 \mu_B$ . This will be also explained in detail in Sec. VII. For the time being we just point out that this behavior is unique to Fe: using similar values of  $U$  for other impurities does not modify their spin moments.

At the level of the GGA calculations Fe constitutes the border between two different characters of the spin mo-

ment associated with the substitutional metal impurities in graphene:  $3d$  magnetism for V-Mn and a “defective-carbon” -like magnetism for heavier atoms. For Co, Ni, the noble metals and Zn the electronic levels close to the  $E_F$  have a stronger contribution from the carbon nearest-neighbors and resemble the levels of the isolated  $D_{3h}$  carbon vacancy. In particular, Mulliken population analysis show that the spin moment of the noble metals impurities has a dominant contribution for the three nearest carbon neighbors (see Table I). For Zn two electrons occupy a two-fold degenerate level reminiscent of the E  $sp$  level of the unreconstructed carbon vacancy (see Sec. IV). As a consequence, the system suffers a Jahn-Teller distortion and has a zero spin moment. However, it is possible to stabilize a symmetric configuration ( $Zn_{C_{3v}}$ ) with a moment of  $2 \mu_B$  and only slightly higher in energy.

#### IV. UNRECONSTRUCTED $D_{3h}$ CARBON VACANCY

We have seen in the previous summary of results that, as substitutional impurities in graphene, most of the metal atoms studied here present a threefold symmetrical configuration. For this reason we have found particularly instructive to analyze their electronic structure as the result of the hybridization between the atomic levels of the metal atoms with the electronic levels associated with an unrelaxed  $D_{3h}$  symmetrical carbon vacancy.

Figure. 4 (a) shows the electronic structure of such  $D_{3h}$  carbon vacancy as calculated using  $4 \times 4$  graphene supercell, while panel (b) presents a simplified scheme that highlights the defect levels associated with the vacancy and indicates their different character and symmetry. The defect levels of the  $D_{3h}$  vacancy can be easily classified according to their  $sp$  or  $p_z$  character and whether they transform according to A or E-type representations. Close to the  $E_F$  we can find a fully symmetric A  $p_z$  level (thus belonging to the  $A_2''$  irreducible representation) and two degenerate (at  $\Gamma$ ) defect levels with E symmetry and  $sp$  character ( $E'$  representation). Approximately 4 eV below  $E_F$  we find another defect level with A  $sp$  character ( $A_1'$  representation).

It is interesting to note that it is not possible to identify any localized defect level with E  $p_z$  ( $E''$ ) character. This is due to the strong coupling with the delocalized states in the graphene layer and contrasts to the case of the A  $p_z$  level. The A  $p_z$  level lies very close to  $E_F$ , where the density of states is low, and due to its A symmetry cannot appreciably couple to the delocalized  $p_z$  states of graphene in that energy range. On the contrary, the E  $p_z$  combinations present a very strong hybridization with the rest of the states of the graphene layer. Indeed, an inspection of the Projected Density of States (PDOS) (see the scheme in Fig. 4 (b)) reveals that the spectral weight associated with such E symmetry linear combinations of  $p_z$  orbitals of the carbon atoms surrounding the vacancy extend over the whole valence and conduction band of

graphene. It is important to take the last observation into account when developing a model of the electronic structure for the metal substitutionals in graphene. Note that we need to have the correct number of electrons from carbon available for forming localized (covalent) bonds.

The three carbon atoms around the vacancy provide three unpaired electrons associated with the unsaturated  $sp$  lobes and three electrons coming from the  $p_z$  orbitals. As shown in Fig. 4 (b), two of these electrons stay in  $p_z$  states delocalized over the graphene layer while the other four electrons fill the A  $sp$  and A  $p_z$  levels localized at the vacancy.

#### V. ANALYSIS OF THE ELECTRONIC STRUCTURE

We now turn to the problem of the electronic structure of  $3d$  transition and noble metal atoms as substitutional impurities in graphene. We first present a model of the hybridization between carbon and metal levels and, subsequently, we show that this model allows to understand in detail the band structures obtained in our calculation for all the metals.

##### A. Sc and Ti: filling the vacancy-metal bonding levels

Figure 5 (a) presents a schematic representation of the hybridization of the  $3d$  levels of Ti with those of an unreconstructed  $D_{3h}$  carbon vacancy. We only consider explicitly the  $3d$  states of the metal atom since our calculations show that, for transition metals, the main contribution from  $4s$  orbitals appears well above  $E_F$ . Due to the symmetric position of the metal atom over the vacancy the system has a  $C_{3v}$  symmetry and the electronic levels can still be classified according to the A or E irreducible representations of this point group. Of course, metal and carbon vacancy states only couple when they belong to the same irreducible representation. Thus, occupied A  $p_z$  and A  $sp$  vacancy levels can only hybridize with the  $3d_{z^2}$  orbitals ( $A_1$  representation), while all the other  $3d$  metal orbitals can only couple to the unoccupied E  $sp$  vacancy levels.

With these simple rules in mind and taking into account the relative energy position of carbon and metal levels, that changes as we move along the transition metal series, we can propose a model of the electronic structure of substitutional transition metals in graphene as represented in Fig. 5 (a) and (b). There are three localized defect levels with  $A_1$  character and three twofold-degenerate levels with E character. Two of these E levels correspond to bonding-antibonding  $sp-d$  pairs, while the third one corresponds to  $3d$  non-bonding states. For Sc-Mn the three  $A_1$  levels can be pictured as a low lying bonding level with A  $sp-d_{z^2}$  character and a bonding-antibonding pair with A  $p_z-d_{z^2}$  character.



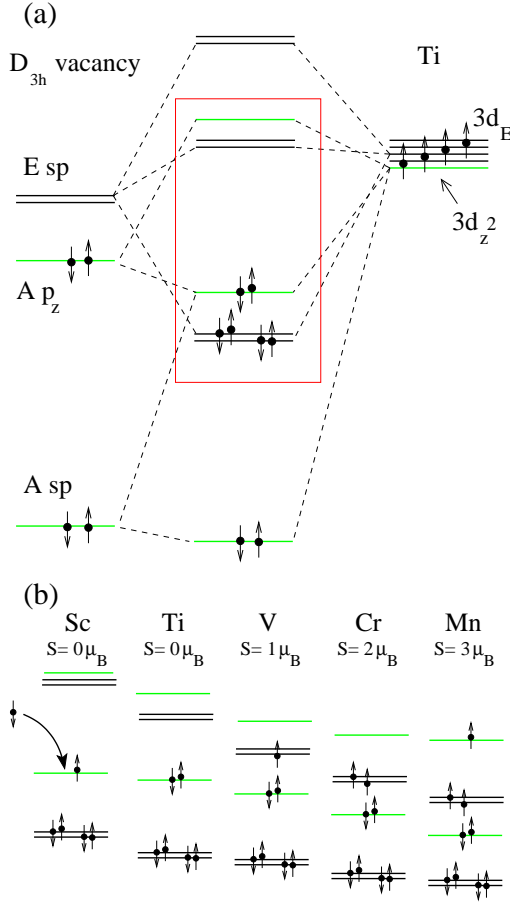


FIG. 5: (Color online) (a) Scheme of the hybridization between the  $3d$  levels of Ti and the localized impurity levels of the  $D_{3h}$  C vacancy. Only  $d$  levels of Ti are taken into account since our calculations show that, at least for transition metals, the main contribution from  $s$  levels appears well above  $E_F$ . Levels with A symmetry are represented by gray (green) lines, while those with E symmetry are marked with black lines. The region close to  $E_F$  is highlighted by a (red) square. (b) Schematic representation of the evolution of the electronic structure near  $E_F$  for several substitutional transition metals in graphene. The spin moment ( $S$ ) is also indicated. Substitutional Sc impurities act as electron acceptors, causing the p-doping of the graphene layer.

Therefore, as shown in Fig. 5 we have four metal-vacancy bonding levels (two A and one doubly-degenerate E levels) that can host up to eight electrons. Ti contributes with four valence electrons, and there are four electrons associated with the localized carbon-vacancy levels. Thus, for Ti the bonding states are completely occupied. Consequently, Ti presents the highest binding energy among all  $3d$  transition metals and has a zero spin moment.

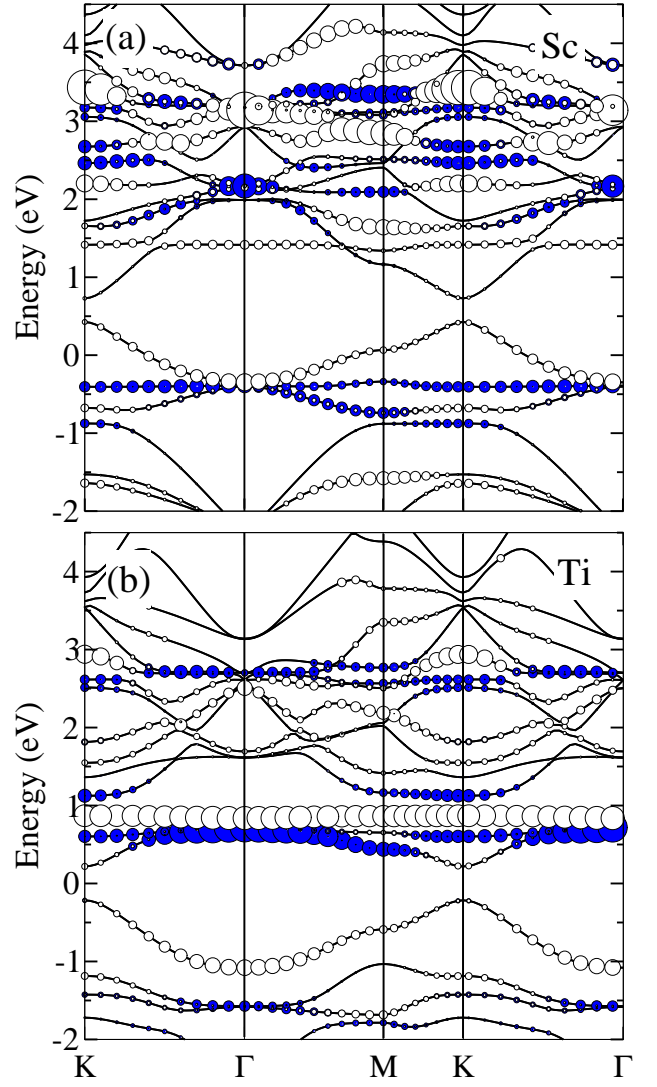


FIG. 6: (Color online) Calculated band structure of substitutional Sc (a) and Ti (b) impurities in  $4 \times 4$  supercell of graphene. Open circles indicate the contribution from  $3d_{z^2}$  orbitals of the metal atom and C  $2p_z$  orbitals of the neighboring C atoms. Solid circles indicate contributions from the rest of the  $3d$  orbitals and C  $2p_x$  and  $2p_y$  orbitals. Energies are referred to the Fermi energy.

The situation for Sc ought to be discussed in detail. As Sc has three valence electrons, in principle we could expect an incomplete filling of the metal-vacancy bonding levels and a spin moment of  $\sim 1 \mu_B$ . However, in our model the highest bonding state (with A  $p_z$ - $d_{z^2}$  character) appears below  $E_F$  and the Sc impurity can act as an acceptor impurity. Our calculations show that this is indeed the case. The Sc-vacancy  $p_z$ - $d_{z^2}$  impurity level captures an electron from the extended states of the graphene layer which becomes p-doped. In total, the substitutional Sc-graphene system does not show any spin polarization.

We can now contrast the expectations from our model

TABLE I: Mulliken population analysis of the spin moment in the central metal impurity ( $S_M$ ) and the carbon nearest neighbors ( $S_C$ ) for different substitutional impurities in graphene.  $S_{tot}$  is the total spin moment in the supercell.

	$S_M (\mu_B)$	$S_C (\mu_B)$	$S_{tot} (\mu_B)$
V	1.21	-0.09	1.0
Cr	2.53	-0.20	2.0
Mn	2.91	-0.10	3.0
Co	0.44	0.06	1.0
Cu	0.24	-0.03, 0.31, 0.31	1.0
Ag	0.06	-0.31, 0.54, 0.54	1.0
Au	0.16	-0.28, 0.50, 0.50	1.0
$Zn_{C_{3v}}$	0.23	0.37	2.0

with actual calculations. Figure 6 shows the band structure of Sc (a) and Ti (b) close to the  $E_F$ . As expected, the main contribution from the 3d shell is found above  $E_F$ . Below  $E_F$  we find one defect band with  $p_z$ - $d_{z^2}$  character and two bands (degenerate at  $\Gamma$ ) with  $sp$ - $d$  character. These bands are in close correspondence with the bonding A and E levels appearing in our model. In the case of Ti the  $E_F$  is located inside a gap of  $\sim 0.5$  eV that opens at K point in the Brillouin zone. This gap appears due to the relatively small  $4 \times 4$  supercell used in these calculations and is reduced when larger supercells are used. Thus, the filling of the graphene extended bands is not appreciably changed by substitutional doping with Ti. For Sc the situation is different. As shown in Fig. 6 (a)  $E_F$  moves away from the K point, the Sc-vacancy complex captures one electron and the graphene layer becomes doped with holes.

Regarding the unoccupied bands, the 3d contribution for Sc above  $E_F$  appears quite broadened due to the strong hybridization with the graphene states. Indeed, the defect levels are somewhat difficult to identify and to correlate with our model. One exception is a flat band with strong  $d_{z^2}$  character appearing at  $\sim 1.5$  eV that, due to its symmetry, does not couple so efficiently with the host states. The case of Ti is much easier to interpret in terms of the simplified model presented in Fig. 5 (a). In particular, we can find two bands at  $\sim 0.6$  eV with strong  $d_{xy}$  and  $d_{x^2-y^2}$  contribution that correspond with the non-bonding  $d$  impurity levels, and one band with  $d_{z^2}$  character at  $\sim 0.8$  eV corresponding with the A  $p_z$ - $d_{z^2}$  antibonding level. Around 2.6 eV we can also find the two E  $sp$ - $d$  antibonding defect levels, although in this case much more hybridized with the host.

### B. V, Cr and Mn: 3d magnetism

As we have seen above, the metal-vacancy bonding levels are completely filled for substitutional Sc and Ti and, as a consequence, the spin moment associated with these impurities is zero. However, following our model in Fig.

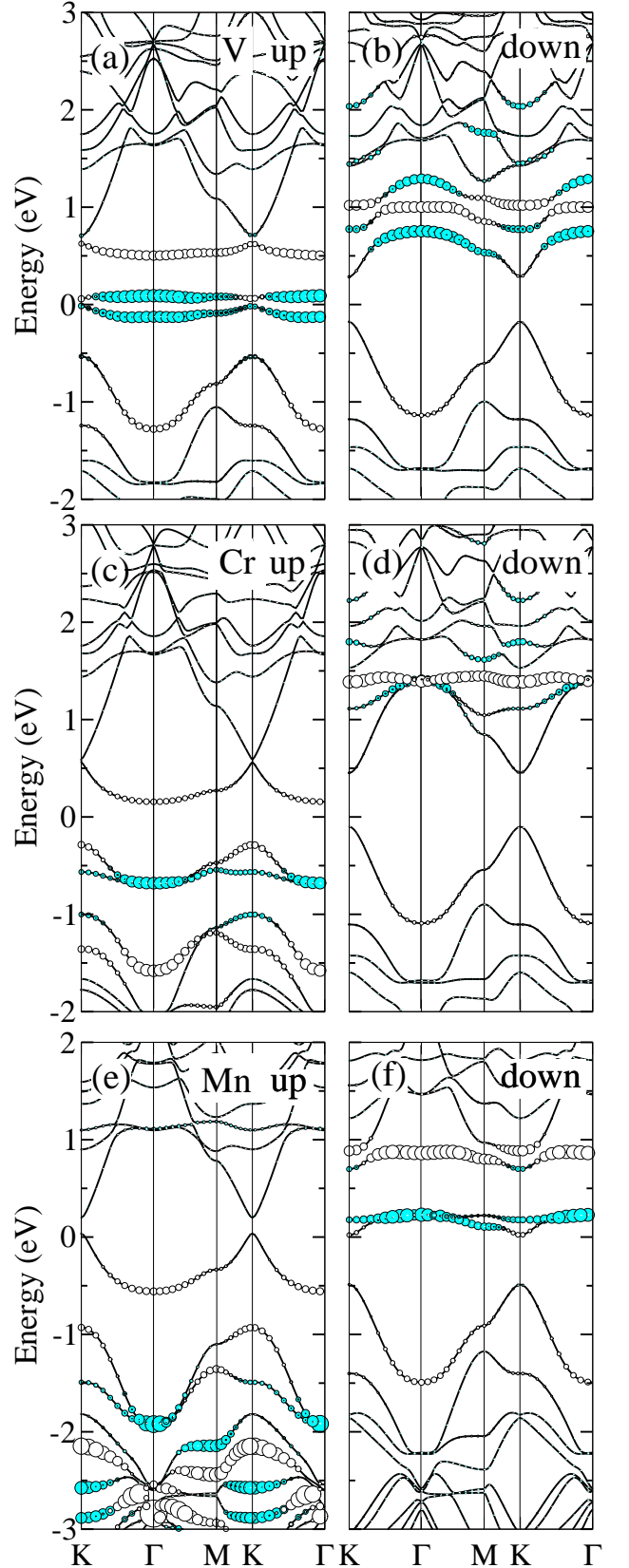


FIG. 7: (Color online) Calculated band structure of substitutional V (panels (a) and (b)), Cr ((c) and (d)) and Mn ((e) and (f)) impurities in a  $4 \times 4$  supercell of graphene. Open and filled circles indicate, respectively, the contribution from  $3d_{z^2}$  and the rest of the 3d orbitals of the metal and, therefore, also indicates levels with A and E symmetries. Energies are referred to the Fermi energy



ures 5 (a) and (b), as we move along the transition metal series the number of valence electrons increases and the non-bonding  $3d$  impurity states start to become occupied. Hence, due to the strong atomic character and localization of these states, the system develops a non-zero spin moment.

Figure 7 shows the calculated band structures for V, Cr and Mn impurities in a  $4 \times 4$  supercell of graphene. The full calculations and the predictions of our simplified model agree remarkably, at least in the neighborhood of  $E_F$ . For V and Cr this correspondence is particularly evident: one and two electrons, respectively, occupy the degenerate non-bonding E  $d$  levels. These non-bonding levels have a dominant contribution from the  $3d_{xy}$  and  $3d_{x^2-y^2}$  orbitals of the metal atoms. As expected, the spin moments associated with these impurities are, respectively, 1 and 2  $\mu_B$ . The strongly localized character of these spin moments is corroborated by the Mulliken population analysis shown in Table I. This analysis indicates that the spin moment is mainly localized at the metal impurity. The contribution from the neighboring carbon atoms is much smaller and has the opposite sign. The localized character of the moment is also consistent with the relatively large values of the spin splitting of the impurity bands. From Figure 7 we calculate a spin splitting of  $\sim 0.9$  eV for V and almost 2 eV for Cr for the E  $d$  levels at  $E_F$ . These splittings are comparable to those of  $d$ -electrons in magnetic bulks, in the order of 1 eV.

Figure 7 (e) and (f) show the majority and minority spin band-structures for Mn substitutionals in graphene. In addition to the non-bonding  $3d$  levels, the antibonding A  $p_z$ - $d_{z^2}$  defect level also becomes occupied and spin-polarized. This level has an important contribution from the  $3d_{z^2}$  state of Mn (given by open symbols). Therefore, it is relatively localized within the Mn atom and presents a significant tendency towards spin polarization. Indeed, our calculations show that Mn substitutions in graphene give rise to a spin moment of 3  $\mu_B$ . The Mulliken decomposition for Mn in Table I confirms again the localized character of this spin moment. However, some differences respect to V and Cr are also found. In those cases, the moment associated with the metal atoms was always larger than the total moment and the only significant additional contributions came from the nearest carbon neighbors. However, for Mn the atomic moment is somewhat smaller (2.91) than the total moment (3.0). Taking into account the contribution from the nearest carbon neighbors (-0.3), a moment of  $\sim 0.4 \mu_B$  is assigned to carbon atoms that are further away from the defect. This indicates a slightly more delocalized character of the spin moment of Mn, since for V and Cr the “long range” contribution was smaller than  $0.1 \mu_B$ . From the band structures in Fig. 7 (e) and (f) we obtain a spin splitting of  $\sim 2.1$  eV for the non-bonding  $d$  levels of the Mn impurity, similar to the case of Cr. The spin splitting for the antibonding A  $p_z$ - $d_{z^2}$  state has a smaller value of  $\sim 1.5$  eV, indicative of its larger spatial extension.

From the simple scheme presented in Fig. 5 (a) we can-

not completely determine the value of the spin moment of the Mn impurity. It can be 3  $\mu_B$  as found in our first principles calculations and schematically depicted in Fig. 5 (b). However, a magnetic moment of 1  $\mu_B$  is also a possible answer. In the latter case, the additional electron in Mn with respect to Cr could populate one of the minority-spin non-bonding  $d$  impurity levels instead of the antibonding A  $p_z$ - $d_{z^2}$  level. In such situation, the spin moment is determined by a delicate balance between the onsite exchange energy within the  $3d$  shell, and the energy cost ( $\Delta\epsilon_{Ad}$ ) to promote one electron from the non-bonding  $d$  levels to the higher energy antibonding A  $p_z$ - $d_{z^2}$  state. Note that the electron-electron repulsion is also reduced when the electron moves into the less localized A  $p_z$ - $d_{z^2}$  level. An estimate of the exchange energy can be obtained from the spin splitting ( $\Delta_S$ ) of the defect levels nearby  $E_F$ . The relative position of the  $3d$  states respect to the A  $p_z$  level of the carbon vacancy and the interaction matrix element between these levels determine  $\Delta\epsilon_{Ad}$ . Thus, within our GGA-DFT calculations we can expect the high spin solution to be favored approximately when  $\Delta_S > \Delta\epsilon_{Ad}$ . From the band structures in Fig. 7 (e) and (f) we obtain  $\Delta\epsilon_{Ad} \sim 1.0$  eV, which is smaller than the values of  $\Delta_S$  discussed previously and, therefore, is consistent with the calculated moment of 3  $\mu_B$  for Mn. Fe impurities considered below in detail present a similar situation where two spin configurations are possible. However, in the case of Fe the low spin (spin compensated) solution is preferred at the level of DFT-GGA calculations as a result of the stronger metal-carbon hybridization.

In short, both the results of the calculations and the expectations based on our model of the metal-vacancy bonding point towards a very strong  $3d$  character of the defect levels appearing nearby of  $E_F$  for V, Cr and Mn substitutional impurities in graphene. The filling of these localized levels favors high spin solutions in accordance with the first Hund’s rule of atomic physics. Thus, we can picture the appearance of spin polarization for V, Cr and Mn substitutionals in graphene as “standard”  $d$ -shell magnetism.

### C. Fe, Co, Ni: strong contribution from the carbon vacancy levels

As we have seen in the previous section the defect levels appearing in the neighborhood of  $E_F$  associated with the presence of V, Cr and Mn substitutional impurities in graphene have a strong  $3d$  character. Consequently, these impurities exhibit large spin moments. However, when increasing the atomic number along the transition series, the atomic  $3d$  levels move to lower energies and we enter a different regime: the defect states nearby  $E_F$  have a predominant contribution from the carbon atoms neighboring the metal impurity. For  $3d$  late transition metals heavier than Fe, the noble metals and Zn we can establish a strong link between the electronic structure

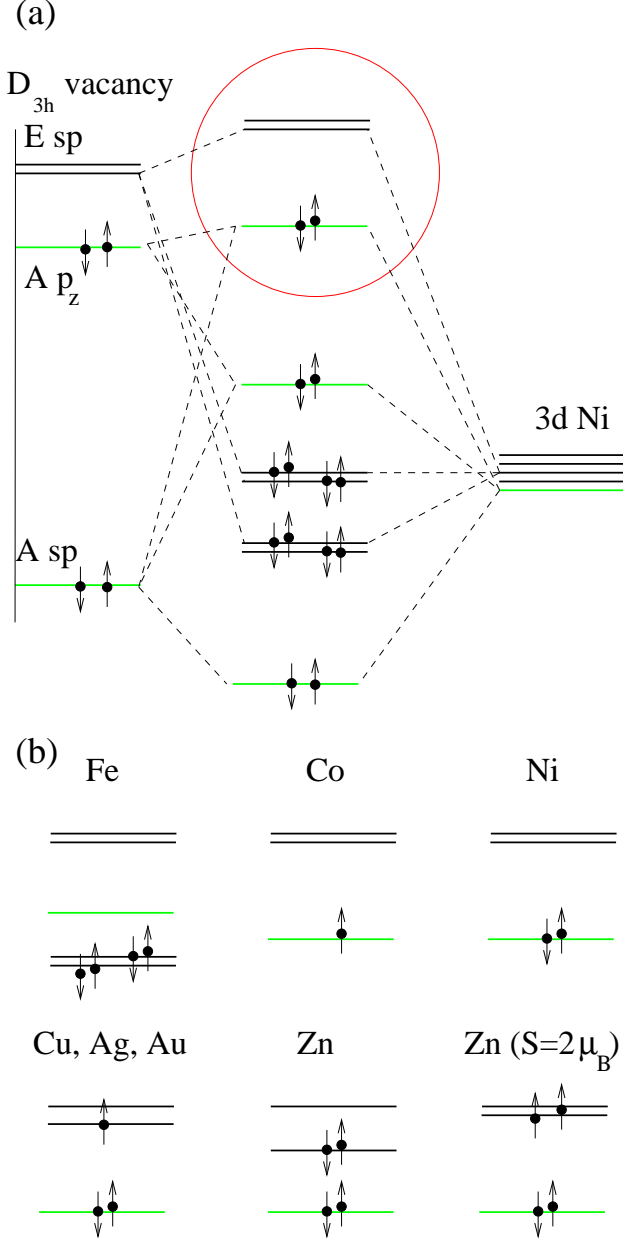


FIG. 8: (Color online) (a) Similar to Fig. 5 (a) for the case of Ni. The region close to the Fermi level is indicated by a (red) circle. (b) Scheme of the levels close the  $E_F$  for Fe, Co, Ni, noble metals and Zn. For Fe, in addition to the antibonding metal-vacancy levels, we have also included the non-bonding  $d$  levels that also appear quite close to  $E_F$ . The noble metals slightly break the  $C_{3v}$  symmetry. For Zn there are two solutions: a high spin solution that preserves symmetry and a distorted one with zero spin moment.

of these impurities around  $E_F$  and that of the unreconstructed  $D_{3h}$  carbon vacancy.

A detailed scheme of the hybridization of the Ni  $3d$  states with those of the carbon vacancy, and the resulting electronic structure, is presented in Fig. 8 (a). All the bonding and non-bonding metal-vacancy states are filled

in this case and the levels appearing closer to  $E_F$  have antibonding character and a strong contribution from the three carbon nearest-neighbors. Closely below  $E_F$  we find a level with A character and a strong C  $2p_z$  contribution and a smaller weight in the Ni  $3d_{z^2}$  state. Above  $E_F$  there are two degenerate levels with E character mainly coming from the C  $2sp$  lobes and hybridized with the Ni  $3d_{xz}$  and  $3d_{yz}$  orbitals. The resulting electronic structure strongly resembles that of the isolated  $D_{3h}$  (unreconstructed) carbon vacancy as can be checked by comparing the band structures in Fig. 4 (a) and Fig. 9 (d). The main difference stems from the slightly higher position of the unoccupied E levels in the case of the Ni impurity. This upward shift is due to the antibonding interaction with the  $d$  states of Ni and contributes to the stability of the  $C_{3v}$  spin-compensated solution. In the case of the  $D_{3h}$  carbon vacancy, the E C  $2sp$  levels lie closer to  $E_F$  and make the system unstable against spin and structural distortions. This clear connection between the electronic structure of Ni and that of the  $D_{3h}$  vacancy was already emphasized in Ref. 22.

Thus, our GGA calculations predict Ni substitutional to be a closed shell system with zero spin moment. One could expect that a better description of the electron-electron interaction within the  $3d$  shell would enhance any tendency of the system towards a magnetic instability. For this reason we have performed GGA+U calculations (using the VASP code) with values of U up to 4.5 eV. However, Ni substitutional impurities in *flat* graphene always remain non-magnetic in the calculations.

In Ref. 22 we proposed a different way to switch on the magnetism of Ni substitutionals: the possibility of spin-moments induced by curvature. The idea consists in lifting the degeneracy of the two unoccupied E  $sp-d$  levels by applying a structural distortion. If the distortion is large enough one of these levels close to  $E_F$  becomes partially populated and, due to its small band width, spin polarized. We have checked that the curvature of the carbon layer in (n,n) nanotubes with n ranging between 4 and 8 induces spin moments as large as  $0.8 \mu_B$  per Ni substitutional impurity. The spin moment in these substitutionally Ni-doped nanotubes is strongly dependent, not only on the layer curvature, but on the density and arrangement of defects in the tube. We have recently demonstrated that a similar switching of the magnetic moment can be obtained in flat Ni-doped graphene by applying adequate structural distortions, thus providing a simple way to control the spin of this system.<sup>44</sup>

As suggested by our scheme in Fig. 8 (b), we can now try to understand the electronic structure of Co and Fe impurities from that of the Ni substitutional but removing, respectively, one and two electrons. According to this image Co substitutionals should present a spin moment of  $1 \mu_B$ , while Fe substitutionals should be non-magnetic. This is indeed confirmed by our GGA calculations.

Figures 9 (b) and (c) show, respectively, the majority and minority spin band structures of the Co impurity. In the neighborhood of  $E_F$  we find a spin-polarized band

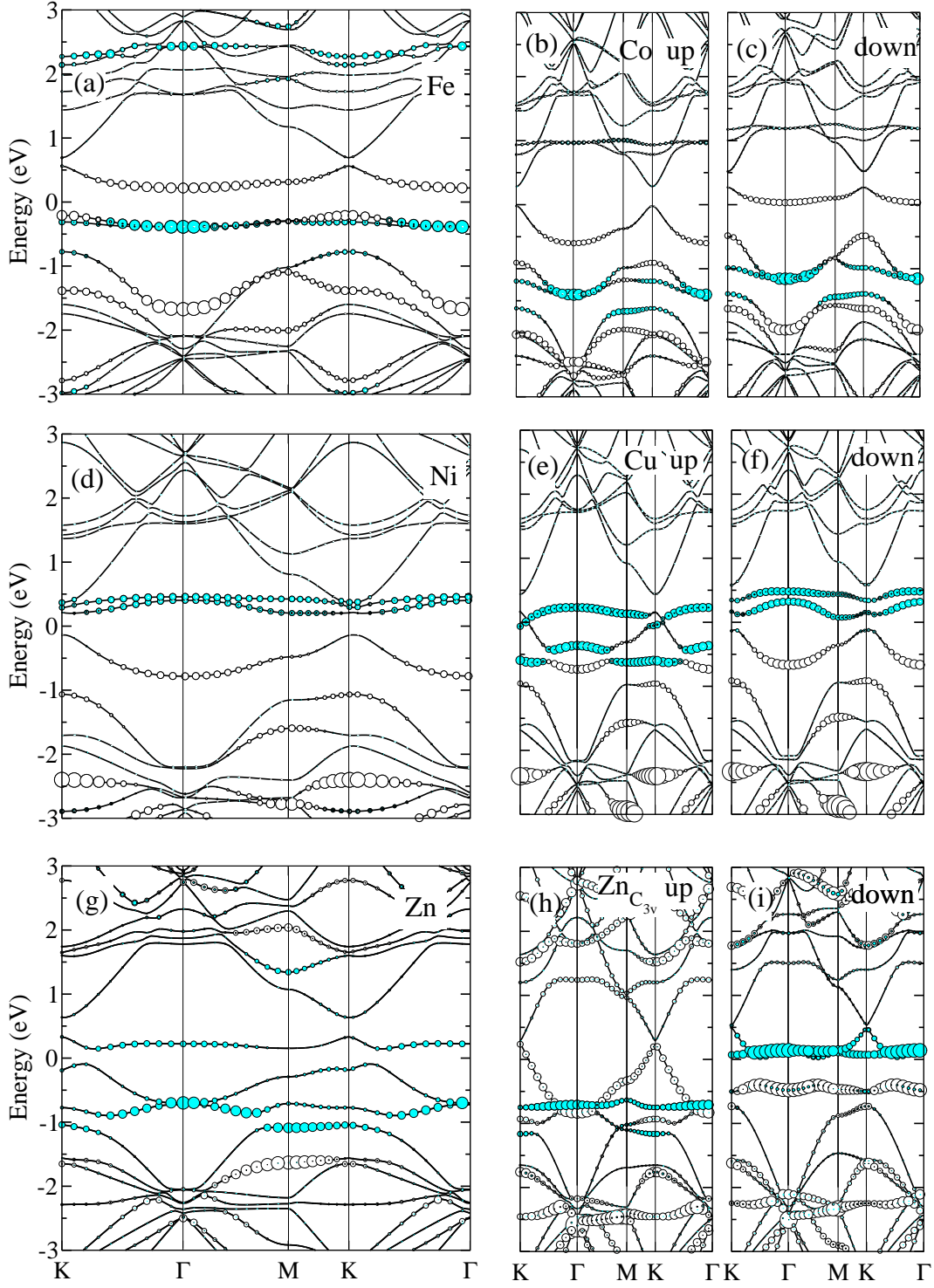


FIG. 9: (Color online) Like Fig. 7 for Fe (a), Co (b) and (c), Ni (d), Cu (e) and (f), Zn (g) and symmetric  $\text{ZnC}_{3v}$  (h) and (i) substitutional impurities in graphene.

associated with the antibonding A  $p_z$ - $d_{z^2}$  impurity level. The spin splitting of this band is  $\sim 0.5$  eV. The hybridization character of this level is confirmed by the Mulliken analysis in Table. I. Only a contribution of  $0.44 \mu_B$  to the total spin moment comes from the Co atom. The

relatively delocalized character of the A  $p_z$ - $d_{z^2}$  level also becomes evident. Only a moment of  $0.18 \mu_B$  comes from the three carbon nearest neighbors, while  $0.38 \mu_B$  comes from carbon atoms at larger distances. The slow distance decay of the A  $p_z$ - $d_{z^2}$  defect level translates into quite

TABLE II: Structural parameters for substitutional noble metals in graphene.

	$d_{C-M}(\text{\AA})$	$h_z(\text{\AA})$	$\theta(^{\circ})$
Cu	1.93, 1.90, 1.90	1.40	88.9, 88.9, 95.2
Ag	2.23, 2.19, 2.19	1.84	71.7, 71.7, 76.7
Au	2.09, 2.12, 2.12	1.71	78.0, 78.0, 81.6

strong and long-range magnetic interactions between moments associated with neighboring Co defects.<sup>28</sup> Indeed, the peculiar electronic structure of the Co impurities has important consequences for the magnetism of this system: couplings show a complex dependence with distance and direction, while the total spin-moment is determined by the number of Co substitutions in each sublattice of the graphene layer. We refer the interested reader to Ref. 28.

Figure 9 (a) presents the GGA band structure for a Fe substitutional defect in a  $4\times 4$  supercell of graphene. Similar results are found using a larger  $8\times 8$  supercell. This band structure is again in reasonable agreement with the simple model presented in Fig. 8. The non-bonding  $d$  levels are completely filled and appear  $\sim 0.4$  eV below  $E_F$  in the vicinity of  $\Gamma$ . The A  $p_z$ - $d_{z^2}$  level is mostly unoccupied and close to 0.2 eV above  $E_F$  near  $\Gamma$ . However, we can see that nearby the K point the  $p_z$ - $d_{z^2}$  band becomes partially occupied, indicating a small charge transfer from the dispersive  $\pi$  bands of graphene to the defect. Mulliken analysis also reflects a small charge accumulation of  $\sim 0.16$  electrons in Fe. In spite of this small partial population, the spin compensated solution is the most stable for Fe substitutionals at the GGA level.

As already pointed out in Sec. III C, the magnetic behavior of the Fe impurity is a consequence of a delicate balance between the onsite electron-electron interaction and the metal-carbon hybridization. For this reason, we devote a whole Section below (Sec. VII) to explore how the band structure and spin moment of Fe substitutionals are modified when these factors are independently controlled by changing the Fe-C bond length and using the GGA+U approximation to describe the effects of the electron-electron repulsion within the  $d$ -shell.

#### D. Noble metals

In the previous sections we have seen that some of the traditional ferromagnets, like Fe and Ni, become non-magnetic as substitutional impurities in graphene. Also quite surprisingly, we find here that substitutional impurities of noble metals are magnetic with a spin moment of  $1 \mu_B$ . The reason for this behavior becomes clear once the electronic structure of these defects is understood.

The band structures can be found in Fig. 9 (e) and (f) for Cu and in Fig. 10 for Ag and Au. In agreement with the predictions of our simplified model in Fig 8, we can see that in the case of the noble-metal impurities

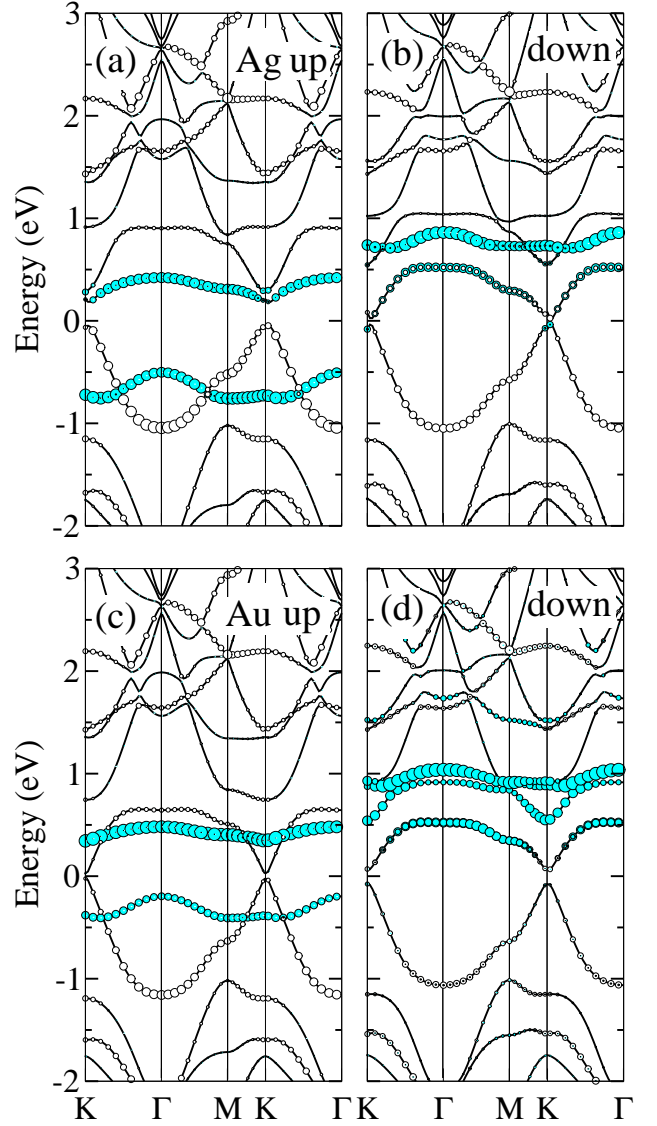


FIG. 10: (Color online) Like Fig. 7 for Ag and Au. The similarities with the band structure of Cu in Fig. 9 are evident.

the two-fold degenerate E  $sp$ - $d$  antibonding levels<sup>45</sup> are now occupied with one electron. The system undergoes a small structural distortion that removes the degeneracy of these levels and the unpaired electron becomes spin polarized. Therefore, substitutional impurities of the noble metals in graphene exhibit a spin moment of  $1 \mu_B$ . Relativistic effects are known to be much more important for Au than for Ag and Cu. Although we have not included spin-orbit coupling in our calculations, scalar relativistic effects are taken into account in the construction of the pseudopotentials. However, the similarities between the electronic structure of all three noble metals are evident, which indicates that bonding and magnetic behavior is mainly dictated by the number of valence electrons.

Structural parameters for all noble metals impurities can be found in Table II. For Cu and Ag one of the metal-carbon bond lengths is slightly larger than the other two,

TABLE III: Structural parameters and binding energies for substitutional Zn impurities in graphene for the symmetric  $C_{3v}$  and most stable distorted configurations.

	$E_B$ (eV)	$d_{C-M}$ (Å)	$h_z$ (Å)	$\theta$ (°)
$Zn_{C_{3v}}$	0.91	1.99	1.67	87.9
Zn	1.07	2.06, 1.89, 1.89	1.54	88.3 88.3 103.9

whereas for Au one is shorter than the others. However, the distortions are rather small with variations of the bond lengths smaller than 2 %. The differences introduced by the larger scalar relativistic effects of Au mainly reflect in the slightly smaller metal-carbon bond length for this metal as compared with Ag.

Table I shows the distribution of the spin moment among the metal atom and the nearest carbon neighbors. We can see that the contribution from the metal atom is almost negligible, particularly in the case of Ag. This can be expected from the lower energy position of the  $d$  shell in the case of the noble metals as compared with transition metals. Although slightly hybridized with the  $p$  shell of the metal impurity, the defect states nearby  $E_F$  in this case are mainly coming from the carbon neighbors. Still the spin moment is rather localized in the complex formed by the metal atom and its three nearest neighbors, which for Cu and Ag contributes with a moment of  $0.83 \mu_B$ , and up to  $0.88 \mu_B$  for Au. The contribution from the rest of the graphene layer is much smaller than, for example, in the case of Co. This reflects the dominant contribution from the relatively localized carbon  $sp$  lobes in the description of the defect states nearby  $E_F$  for these impurities. This analysis reinforces the link with the electronic structure of the unreconstructed  $D_{3h}$  carbon vacancy in graphene as presented in Sec. V C. In fact, we can picture the main role of late transition- and noble-metals substitutionals in graphene as to stabilize the structure of the carbon monovacancy, that otherwise will severely reconstruct, and to change its charge state.

## VI. JAHN-TELLER DISTORTION OF SUBSTITUTIONAL ZN

For Zn impurities a second electron is added to the two-fold degenerate  $E$   $sp-d$  shell. Under these circumstances two scenarios are possible: (i) a non-magnetic solution in which the system has undergone a Jahn-Teller-like distortion, or (ii) a high-spin solution that maintains the symmetric  $C_{3v}$  geometry of the defect. The relative energy of both solutions depends on the balance between the energy gain associated with the distortion and the exchange energy of the electrons. Both types of solutions are obtained in our density functional calculations for Zn substitutional impurities in graphene.

The details of the structure and the binding energies of the Zn impurity are presented in Table III as calculated with SIESTA. Very similar results are obtained for

both configurations using VASP. The distorted configuration presents one larger Zn-C bond (by  $\sim 3.5\%$ ) and two shorter bonds ( $\sim 5\%$ ) compared with the bond length (1.99 Å) of the undistorted geometry. The distorted configuration is more stable by 160 meV (120 meV using VASP). This rather small energy difference between the two configurations might point to the appearance of non-adiabatic electronic effects at room temperature.

The band structure for both configurations of Zn substitutionals can be found in Fig. 9. Again they confirm the model presented in Fig. 8. The distorted Zn [Fig. 9 (g)] breaks the degeneracy of the  $E$   $sp-d$  levels: one of them appears fully occupied  $\sim 0.8$  eV below  $E_F$ , while the other appears a few tenths of eV above  $E_F$ . For the  $C_{3v}$  Zn impurity both  $E$   $sp-d$  bands are degenerate and the splitting between majority and minority levels is  $\sim 0.71$  eV. Table I shows the Mulliken population analysis of the spin moment for the  $C_{3v}$  Zn systems. As in the case of the noble metals the contribution from the three nearest carbon neighbors is the most important. However, the contribution of Zn is somewhat larger and the total spin moment is more delocalized with a contribution from the rest of the graphene layer of  $\sim 0.66 \mu_B$ . We should note that here we have one additional electron as compared to the noble metal systems.

## VII. FE SUBSTITUTIONALS: COMPETITION BETWEEN INTRA-ATOMIC INTERACTIONS AND METAL-CARBON HYBRIDIZATION

We have already pointed out that Fe substitutionals in graphene occupy a rather special place at the border between two well defined regimes (see Fig. 3): (i) the strong  $3d$  character of the defect levels nearby  $E_F$  and large spin moments found for V, Cr and Mn impurities, and (ii) the larger carbon character of those electronic levels and the small oscillatory spin-moments of Co, Ni and the noble metals. GGA calculations [Fig. 9 (a)] locate Fe impurities within the second group, with all the  $3d$  non-bonding levels fully occupied and non-magnetic. Thus, the spin moment drops from  $3 \mu_B$  for Mn impurities to zero for Fe, showing a quite discontinuous behavior as a function of the number of valence electrons. In analogy with the standard Slater-Pauling rule for transition metals, one could expect to find a more gradual decrease of the spin moment as the number of valence electrons is increased, i.e. Fe would have a moment of  $2 \mu_B$ . In the present section we study in detail why the non-magnetic solution is more stable for Fe.

### A. Key parameters: metal-carbon hopping and intra-atomic Coulomb interactions

Figure 11 shows a scheme of the electronic structure of both Mn and Fe defects. Depending on how electrons are arranged among the  $A$   $p_z-d_{z^2}$  antibonding level and the



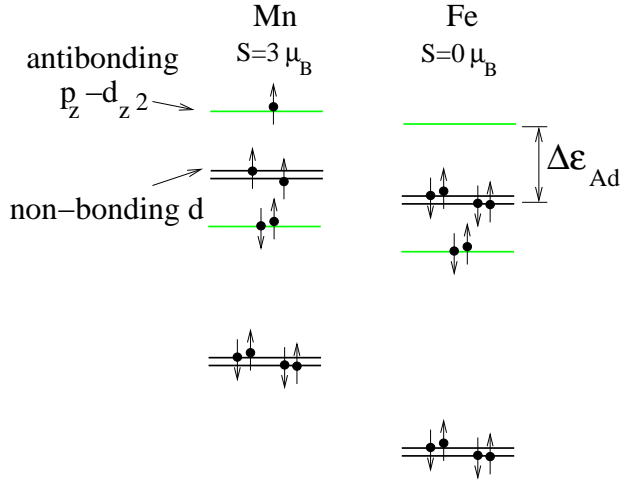


FIG. 11: (Color online) Scheme of the electronic levels near  $E_F$  for Mn and Fe substitutionals in graphene as deduced from our model of bonding and GGA calculations.  $\Delta\epsilon_{Ad}$  is the energy cost to promote an electron to the antibonding A  $p_z$ - $d_{z^2}$  hybridization level from the non-bonding 3d states. The magnitude of  $\Delta\epsilon_{Ad}$ , relative to that of the spin-splitting  $\Delta_S$  of these defect levels, is crucial to determine the spin state of these impurities.

non-bonding 3d states, Mn can exhibit spin moments of  $3 \mu_B$  or  $1 \mu_B$ , while Fe can have a moment of  $2 \mu_B$  or can be non-magnetic. At the GGA level Mn prefers the high-spin configuration, while the low-spin one is more stable for Fe. As commented in Section VB, the relative stability of the different spin states depends on the balance between the effects of Coulomb repulsion and exchange within the 3d levels and the relative energy position of the impurity levels given by  $\Delta\epsilon_{Ad}$  (see Fig. 11). The hybridization with the neighboring C atoms is crucial in this interplay since it influences (i) the degree of localization of the defect levels and the screening of Coulomb interactions, which modify the spin splitting of the electronic levels  $\Delta_S$ , and (ii) the value of  $\Delta\epsilon_{Ad}$  through the effective hopping parameter between the 3d states and the A  $p_z$  carbon vacancy level. Next, we shall deal with both aspects for substitutional Fe in graphene.

### 1. Changing Fe-graphene hopping with distance

By tuning the interaction with the host structure it should be possible to change the spin moment of these impurities. We can modify the hopping by artificially changing Fe-graphene distance. The results of such calculation are shown in Fig. 12 (a). While maintaining the three-fold symmetry of the system, we have performed a series of calculations by progressively increasing the height of the Fe atom over the graphene layer. Increasing the C-Fe bond length by  $\sim 9\%$  we observe an abrupt

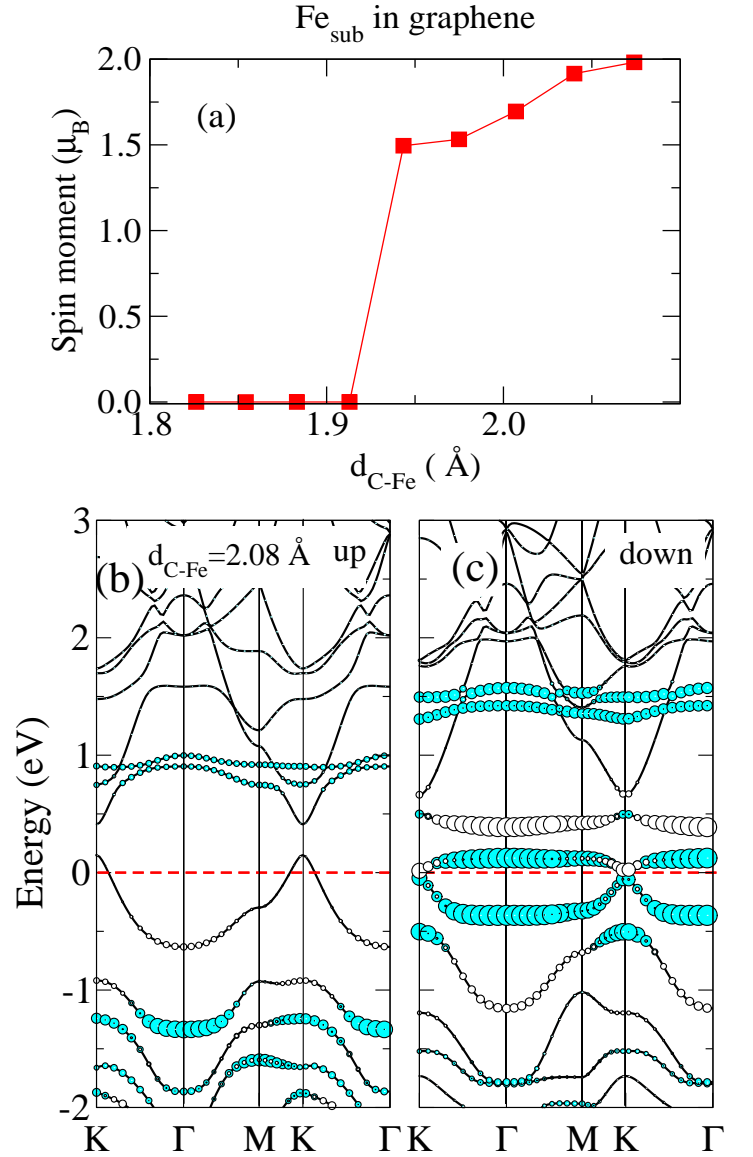


FIG. 12: (Color online) Panel (a) shows the spin moment of a substitutional Fe impurity in graphene as a function of the C-Fe bond length. Equilibrium position corresponds to  $d_{C-Fe} = 1.78 \text{ \AA}$ . Panels (b) and (c) show the band structure for  $d_{C-Fe} = 2.08 \text{ \AA}$ . Symbol code similar to Fig. 7. Energies referred to the Fermi level (indicated by a dashed line).

jump of the spin moment from zero to  $1.5 \mu_B$ . The spin moment continues to rise and saturates at a value of  $2.0 \mu_B$  for  $d_{C-Fe} \sim 2.07 \text{ \AA}$ . This convincingly shows that the metal-carbon hybridization is the key parameter to explain the non-magnetic state of Fe substitutional impurity in graphene. When increasing the C-Fe distance we mainly decrease  $\Delta\epsilon_{Ad}$ . Thus, we reduce the energy penalty for promoting electrons from the non-bonding  $d$  to the A  $p_z$ - $d_{z^2}$  defect levels. At the same time we also increase the atomic character of the non-bonding  $d$  states and reduce the effect of the screening due to the electrons in the graphene layer. This  $\Delta\epsilon_{Ad}$  reduction promotes the

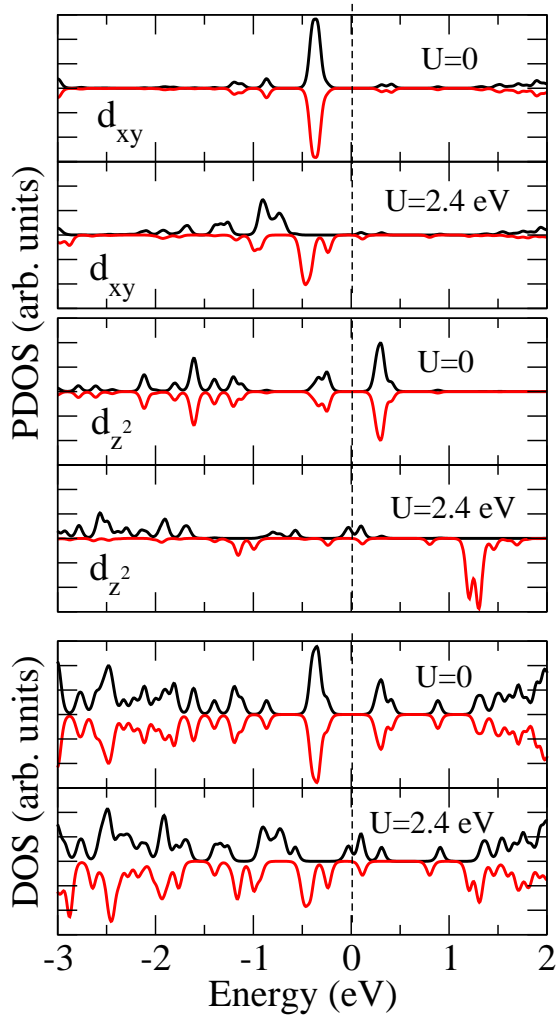


FIG. 13: (Color online) Projected density of states (PDOS) and total density of states (DOS) for a Fe substitutional impurity in graphene calculated with VASP using GGA and GGA+U with  $U=2.4$  eV. Positive (negative) values for majority (minority) spin. When  $U=0$  the system shows zero spin-polarization and the Fe  $3d_{z^2}$  state is partially occupied. A large enough Hubbard  $U$  forces an integer population of the Fe  $3d_{z^2}$  state and produces a spin moment of  $1 \mu_B$ .

electron-electron repulsion within the  $3d$  states of Fe and, eventually, stabilizes the solution with  $2.0 \mu_B$ .

Figures 12 (b) and (c) present the band structure for the high-spin state of Fe, where the C-Fe bond length has been elongated up to  $2.08 \text{ \AA}$ . We notice the differences with the spin-compensated ground state in Fig. 9 (a). On the one hand, one electron is promoted from the non-bonding  $d$  states to the more delocalized antibonding A  $p_z$ - $d_{z^2}$  impurity level in order to reduce the effect of electron-electron repulsion. On the other hand, the spin moment is maximized in accordance with Hund's first rule.

Therefore, we have seen that the non-magnetic character of the Fe substitutionals in the GGA calculations

is due to the larger interaction with the graphene layer, as compared for example with the Mn impurity. This is consistent with the fact that Fe, together with Co and Ni, presents the smaller carbon metal bond length among the whole series of  $3d$  transition metals. Fe impurities also have one of the largest binding energies. By artificially reducing this interaction it could be possible to obtain magnetic Fe substitutional impurities in graphene.

## 2. Changing intra-atomic Coulomb interaction $U$

Another route to explore would be to increase the size of intra-atomic electron-electron interactions. We have done that by using the so-called GGA+U methodology in which a Hubbard term is explicitly added to the DFT Hamiltonian and solved within the mean-field approximation. Our results indicate that with a reasonable value of  $U$  ( $\sim 2$  eV or larger) we obtain a magnetic solution for Fe substitutionals. However, contrary to our initial expectation this solution does not correspond to the  $2 \mu_B$  high-spin solution discussed above, but to a new solution with  $1 \mu_B$ . The key reason to understand this behavior is the partial occupation of the Fe  $3d_{z^2}$  state at the level of GGA calculations. The  $d_{z^2}$  state is strongly coupled to the delocalized A  $p_z$  vacancy level appearing nearby  $E_F$  and both, this hybridization and the population of the atomic orbital, are strongly modified when the value of  $U$  is increased.

Figure 13 shows the results of the electronic structure of Fe impurities calculated using GGA+U with  $U=2.4$  eV and compared with those with  $U=0$ . The two upper panels show the projected density of states (PDOS) onto the  $d_{xy}$  orbital (the projection onto the  $d_{x^2-y^2}$  orbital is identical by symmetry), the two middle panels show the PDOS onto the  $d_{z^2}$  orbital of Fe and the two lower panels show the total density of states. At the level of GGA, with  $U=0$ , there is a very well defined peak closely below  $E_F$  in the  $d_{xy}$  PDOS corresponding to the position of the non-bonding  $d$  states. The spectral weight coming from the  $d_{z^2}$  orbital is more spread: presents some broad structure around  $-1.5$  eV corresponding to the bonding A  $p_z$ - $d_{z^2}$  defect level interacting with the valence band of graphene, and a narrower peak near  $E_F$  with origin in the slightly occupied antibonding A  $p_z$ - $d_{z^2}$  impurity state. Therefore, from the Fe  $3d$  states appearing nearby  $E_F$  we can picture the  $d_{xy}$  and  $d_{x^2-y^2}$  states as fully occupied and the  $d_{z^2}$  as partially occupied due to the larger interaction with the carbon neighbors.

For a sufficiently large value of  $U$  the C  $2p_z$ - $3d_{z^2}$  hybridization is overcome by the tendency of the electrons to have an integer population within the localized  $3d$  shell. Thus, the  $3d_{z^2}$  localizes one electron and, as a consequence, the system develops a  $1 \mu_B$  spin-polarization. This changes can be appreciated in Fig. 13. The majority-spin  $3d_{z^2}$  PDOS shifts downwards, while a strong unoccupied peak appears around  $1.5$  eV in the  $3d_{z^2}$  minority spin PDOS. Simultaneously, a more delocalized

level mostly coming from the  $2p_z$  orbitals of the neighboring C atoms appears half-filled at  $E_F$ . Note that other levels, such as the  $d_{xy}$ , do not suffer such strong modifications since they are already almost fully occupied with  $U=0$ . It is also interesting to note that, due to symmetry considerations, they couple with the graphene layer very differently from the  $d_{z^2}$  level.

### B. Relevance for recent experiments of Fe implantation in graphite

There are recent reports on the paramagnetism of iron-implanted graphite that indicate the existence of local magnetic moments associated with the implanted Fe atoms.<sup>46,47</sup> This would be in contradiction with the present GGA results if we assume that the Fe atoms are incorporated to the graphene layer as substitutionals. However, the final geometry of the implanted atoms in these experiments is not known. Furthermore, a considerable amount of defects is created during the implantation process. Although it has been argued that a large part of the damage is healed by vacancy-interstitial recombination,<sup>47</sup> the influence of these defects, specially interstitials and big voids, on the observed magnetic response can be determinant.

Therefore, it is not fully clear if we can compare our calculations for Fe substitutional impurities in an otherwise perfect graphene layer with these experimental data. However, as we have shown in detail in this section, Fe substitutionals are very close to a transition and, depending on the details of the calculations, it is possible to obtain a magnetic ground state. In particular, Fe substitutionals develop a spin moment of  $1 \mu_B$  at the level of GGA+U calculations for reasonable values of the U parameter. This might be an indication that the non-magnetic ground state found in GGA calculations is a consequence of the limitations of the used functionals.

## VIII. CONCLUSIONS

We have presented a DFT study of the structure, energetics, and electronic and magnetic properties of several metal atoms as substitutional impurities in graphene, i.e., bound to a carbon monovacancy in the layer. We have considered the cases of all  $3d$  transition metals, noble metals and Zn. We have paid special attention to their electronic and magnetic properties and develop a simple model to understand the observed trends. Our model is based on the hybridization of the states of the metal atoms with those of an unreconstructed carbon vacancy. The main ingredients of the model are the assumption, after our calculations, of a three-fold symmetric bonding configuration and the approximate knowledge of the relative energy positions of the levels of the carbon monovacancy and the  $d$  shell of the metal impurity as we move along the transition series. With this model we can un-

derstand the observed variations of the electronic structure of the defect, the size and localization of the spin moment, and the binding energy. We have identified three different regimes corresponding to filling of carbon-metal hybridization shells with different character: bonding, non-bonding and antibonding.

In more detail:

(i) Most substitutional metal impurities present an almost perfectly symmetric three-fold configuration with  $C_{3v}$  symmetry. Noble metals slightly depart from this perfect configuration. Only Zn presents a considerable structural distortion.

(ii) For Sc and Ti the metal-carbon bonding shell is completely filled. Therefore, these impurities present the highest binding energies and zero spin moments. Sc substitutionals act as p-dopants for graphene: each Sc impurity localizes one extra electron from the carbon layer.

(iii) The non-bonding  $d$  shell becomes partially populated for V, Cr and Mn, which develop a very localized spin-moment of 1, 2 and  $3 \mu_B$ , respectively. The binding energy decreases slightly as the  $d$  shell moves to lower energies, thus reducing its hybridization with the higher carbon vacancy levels.

(iv) For Co, Ni, the noble metals and Zn, the metal-carbon levels are progressively populated. This gives rise to an oscillatory behavior of the spin moment between 0 and  $1 \mu_B$ . The spin moments are more delocalized than those found for V, Cr and Mn and present a considerable contribution from the carbon atoms around the impurity. The binding energy presents a local maximum for Co, but suddenly drops for the noble metals and has its minimum for Zn.

(v) The electronic structure, nearby  $E_F$ , of substitutional impurities of Co, Ni, the noble metals and Zn has a strong resemblance to that of the unreconstructed  $D_{3h}$  carbon monovacancy. We can draw an analogy between the electronic structure of these impurities and that of the unreconstructed  $D_{3h}$  carbon monovacancy with different number of electrons (charge states). The spin moment of these impurities can be fully understood exploiting this equivalence. In particular, the result that noble metals develop a spin moment of  $1 \mu_B$  emerges naturally within this picture.

(vi) For the Co impurity, the equivalence can be pushed a step further and we can draw an analogy with the electronic structure of a  $\pi$ -vacancy in a simple  $\pi$ -tight-binding description of graphene. This can be used to explain the peculiar behavior found for the magnetic couplings between Co substitutionals in graphene.<sup>28</sup>

(vii) Fe impurities occupy a distinct position at the border between two different regimes. Their magnetic behavior stems from the competition between the carbon-metal hybridization and the electron-electron interaction within the  $3d$  shell. As a result, although Fe impurities are non-magnetic at the GGA level, GGA+U calculations with moderate values of U (above  $\sim 2$  eV) produce a spin-moment of  $1 \mu_B$ .

(viii) We have found that the unexpected result that

Au substitutionals<sup>29,30</sup> present a spin moment of  $1\mu_B$  also holds for all noble metals, i.e., also Ag and Cu present a  $1\mu_B$  spin moment.

(ix) We have found that the ground state of the Zn substitutional is non-magnetic due to a Jahn-Teller distortion. Yet, it is possible to stabilize a symmetric configuration with a spin moment of  $2\mu_B$  with a very small energy penalty of  $\sim 150$  meV.

In summary, substitutional impurities of metals in graphene present some interesting magnetic and electronic properties and, therefore, can provide an interesting route to add functionalities or to tune the response of devices based on graphenic materials. Furthermore, recent experiments by Rodriguez-Manzo and Banhart<sup>25</sup> have demonstrated the possibility to create individual vacancies at desired locations in carbon nanotubes using electron beams. This ability, in combination with the high stability of substitutional impurities, can open a route to fabricate ordered arrays of these impurities at predefined locations. Such devices would allow, among other applications, the experimental verification of the theoretical predictions of unusual magnetic interactions mediated by graphene.<sup>26,27,28</sup>

## APPENDIX A: PSEUDOPOTENTIALS AND BASIS ORBITALS RADII

For the SIESTA calculations we have used Troullier-Martins norm-conserving pseudopotentials<sup>41</sup> generated using the pseudization radii shown in Table IV of this Appendix. The pseudopotentials for the metal atoms include nonlinear core corrections<sup>42</sup> for exchange and correlation. The pseudocore radii ( $r_{core}$ ) have been optimized for each element. These pseudopotentials have been tested to reproduce the correct results in bulk phases.

For most elements, the shape and radii of the basis sets of numerical atomic orbitals (NAOs) used with SIESTA were determined automatically by the code using an *energy shift* parameter of 50 meV.<sup>35,37</sup> However, for some metal atoms the binding energies were slightly overestimated using these basis sets, mainly due to the confinement of the free atom. For those atoms we enlarged the radii of the basis orbitals (using smaller values of the *energy shift* parameter) until binding energies were converged within a few tens of meV. The largest radius for each element and  $l$  channel is shown in Table V. Notice that double- $\zeta$  polarized (DZP) basis of these metals include a  $p$  shell. In this case the radii of  $p$  orbitals is taken equal to that of the  $s$  shell.

## ACKNOWLEDGMENTS

We acknowledge support from Basque Departamento de Educación and the UPV/EHU (Grant No. IT-366-07),

the Spanish Ministerio de Educación y Ciencia (Grant No. FIS2007-66711-C02-02) and the ETORTEK pro-

TABLE IV: Cutoff radii (in Bohrs) used for the generation of the Troullier-Martins<sup>41</sup> norm-conserving pseudopotentials used in the SIESTA calculations.  $r_l$  stands for the cut-off radius used for the  $l$  channel, while  $r_{core}$  is the matching radius used for the construction of pseudocores in order to include nonlinear core corrections for exchange and correlation<sup>42</sup>.

	Valence	$r_s$ ( $a_o$ )	$r_p$ ( $a_o$ )	$r_d$ ( $a_o$ )	$r_{core}$
Sc	[Ar] $4s^1 3d^2$	3.30	3.30	1.44	0.89
Ti	[Ar] $4s^1 3d^3$	2.96	2.96	1.45	0.72
V	[Ar] $4s^1 3d^4$	2.40	2.79	1.46	0.69
Cr	[Ar] $4s^1 3d^5$	2.51	2.80	1.46	0.65
Mn	[Ar] $4s^1 3d^6$	2.51	2.77	1.45	0.60
Fe	[Ar] $4s^1 3d^7$	2.10	2.10	1.68	0.67
Co	[Ar] $4s^2 3d^7$	2.37	2.48	1.68	0.67
Ni	[Ar] $4s^2 3d^8$	1.85	1.95	1.45	0.53
Cu	[Ar] $4s^1 3d^{10}$	2.33	2.30	1.79	0.53
Ag	[Kr] $5s^1 4d^{10}$	2.45	2.58	2.00	0.83
Au	[Xe] $4f^{14} 6s^1 5d^{10}$	2.55	2.68	2.20	0.93
Zn	[Ar] $4s^2 3d^{10}$	2.04	2.21	1.66	0.49
C	[He] $2s^2 2p^2$	1.25	1.25	1.25	–

TABLE V: Cutoff radii (in Bohrs) of the numerical atomic orbitals (NAOs) used in SIESTA as a basis set. Radii used for the  $s$  and polarization  $p$  shell are equal.

	$r_{sp}^{NAO}$ ( $a_o$ )	$r_d^{NAO}$ ( $a_o$ )
Co	8.00	4.73
Ni	10.94	6.81
Cu	8.87	5.52
Ag	10.48	6.52
Au	8.63	6.08
Zn	9.24	5.33

gram funded by the Basque Departamento de Industria and the Diputación Foral de Guipuzcoa. EJGS would like to thank N. González-Lakunza for valuable help with the VASP code.

- 
- \* Electronic address: eltonjose.gomes@ehu.es  
† Electronic address: swxayfea@ehu.es  
‡ Electronic address: sqbsapod@ehu.es
- <sup>1</sup> A. K. Geim and K. S. Novoselov, *Nature Mat.* **6**, 183 (2007).
  - <sup>2</sup> A. H. Castro Neto, F. Guinea, N. M. Peres, K. S. Novoselov, and A. K. Geim, *Rev. Mod. Phys.* **81**, 109 (2009).
  - <sup>3</sup> K. S. Novoselov et al., *Nature (London)* **438**, 197 (2005).
  - <sup>4</sup> M. I. Katsnelson, K. S. Novoselov, and A. K. Geim, *Nature Physics* **2**, 620 (2006).
  - <sup>5</sup> C. Park, Y.-W. Son, M. L. Cohen, and S. G. Louie, *Nature Physics* **4**, 213 (2008).
  - <sup>6</sup> P. Avouris, Z. Chen, and V. Perebeinos, *Nature Nanotechnology* **2**, 605 (2007).
  - <sup>7</sup> B. Trauzettel et al., *Nature Phys.* **3**, 192 (2007).
  - <sup>8</sup> Y.-W. Son, M. L. Cohen, and S. G. Louie, *Nature* **444**, 347 (2006).
  - <sup>9</sup> O. V. Yazyev and M. I. Katsnelson, *Phys. Rev. Lett.* **100**, 047209 (2008).
  - <sup>10</sup> L. E. Hueso et al., *Nature* **445**, 410 (2007).
  - <sup>11</sup> P. Esquinazi, D. Spemann, D. Höhne, A. Setzer, K.-H. Han, and T. Butz, *Phys. Rev. Lett.* **91**, 227201 (2003).
  - <sup>12</sup> P. O. Lehtinen, A. S. Foster, A. Ayuela, A. V. Krashenninikov, K. Nordlund, and R. Nieminen, *Phys. Rev. Lett.* **91**, 017202 (2003).
  - <sup>13</sup> P. O. Lehtinen, A. S. Foster, Y. Ma, A. V. Krashenninikov, and R. Nieminen, *Phys. Rev. Lett.* **93**, 187202 (2004).
  - <sup>14</sup> T. Makarova and F. Palacios, eds., *Carbon Based Magnetism* (Elsevier, Amsterdam, 2006).
  - <sup>15</sup> A. V. Krashinnikov and F. Banhart, *Nature Mat.* **6**, 723 (2007).
  - <sup>16</sup> B. Uchoa et al., *Phys. Rev. Lett.* **101**, 026805 (2008).
  - <sup>17</sup> O. V. Yazyev, *Phys. Rev. Lett.* **101**, 037203 (2008).
  - <sup>18</sup> J. F.-R. J. J. Palacios and L. Brey, *Phys. Rev. B* **77**, 195428 (2008).
  - <sup>19</sup> J. Fernández-Rossier and J. J. Palacios, *Phys. Rev. Lett.* **99**, 177204 (2007).
  - <sup>20</sup> Y. Gan, L. Sun, and F. Banhart, *Small* **4**, 587 (2008).
  - <sup>21</sup> M. Ushiro, K. Uno, T. Fujikawa, Y. Sato, K. Tohji, F. Watari, W. J. Chun, Y. Koike, and K. Asakura, *Phys. Rev. B* **73**, 144103 (2006).
  - <sup>22</sup> E. J. G. Santos, A. Ayuela, S. B. Fagan, J. M. F. and D. L. Azevedo, A. G. S. Filho, and D. Sánchez-Portal, *Phys. Rev. B* **78**, 195420 (2008).
  - <sup>23</sup> F. Banhart, J. C. Charlier, and P. M. Ajayan, *Phys. Rev. Lett.* **84**, 686 (2000).
  - <sup>24</sup> M. S. Dresselhaus, G. Dresselhaus, and P. Avouris, eds., *Carbon Nanotubes: Synthesis, Structure, Properties and Applications* (Springer, Berlin, 2001).
  - <sup>25</sup> J. A. Rodríguez-Manzo and F. Banhart, *Nano Letters* **9**, 2285 (2009).
  - <sup>26</sup> L. Brey, H. A. Ferting, and S. D. Sarma, *Phys. Rev. Lett.* **99**, 116802 (2007).
  - <sup>27</sup> D. F. Kirwan et al., *Phys. Rev. B* **77**, 085432 (2008).
  - <sup>28</sup> E. J. G. Santos, D. Sánchez-Portal, and A. Ayuela (2009), *cond-mat/0906.5604*.
  - <sup>29</sup> A. V. Krashenninikov, P. O. Lehtinen, A. S. Foster, P. Pyykkö, and R. M. Nieminen, *Phys. Rev. Lett.* **102**, 126807 (2009).
  - <sup>30</sup> S. Malola, H. Häkkinen, and P. Koskinen, *Appl. Phys. Lett.* **94**, 043106 (2009).
  - <sup>31</sup> D. W. Boukhalov and M. I. Katsnelson, *Appl. Phys. Lett.* **95**, 023109 (2009).
  - <sup>32</sup> I. Suarez-Martinez and C. P. Ewels (2009), private communication.
  - <sup>33</sup> J. P. Perdew, K. Burke, and M. Ernzerhof, *Phys. Rev. Lett.* **77**, 3865 (1996).
  - <sup>34</sup> D. Sánchez-Portal, P. O. E. Artacho, and J. M. Soler, *Int. J. Quantum Chem.* **65**, 453 (1997).
  - <sup>35</sup> J. M. Soler, E. Artacho, J. D. Gale, A. García, J. Junquera, P. Ordejón, and D. Sánchez-Portal, *J. Phys.: Condensed Matter* **14**, 2745 (2002).
  - <sup>36</sup> D. Sánchez-Portal, P. Ordejón, and E. Canadell, *Structure and Bonding* **113**, 103 (2004).
  - <sup>37</sup> J. Junquera, O. Paz, D. Sánchez-Portal, and E. Artacho, *Phys. Rev. B* **64**, 235111 (2001).
  - <sup>38</sup> G. Kresse and J. Hafner, *Phys. Rev. B* **47**, 558 (1993).
  - <sup>39</sup> G. Kresse and J. Furthmüller, *Phys. Rev. B* **54**, 11169 (1996).
  - <sup>40</sup> H. J. Monkhorst and J. D. Pack, *Phys. Rev. B* **13**, 5188 (1976).
  - <sup>41</sup> N. Troullier and J. L. Martins, *Phys. Rev. B* **43**, 1993 (1991).
  - <sup>42</sup> S. G. Louie, S. Froyen, and M. L. Cohen, *Phys. Rev. B* **26**, 1738 (1982).
  - <sup>43</sup> S. L. Dudarev, G. A. Botton, S. Y. Savrasov, C. J. Humphreys, and A. P. Sutton, *Phys. Rev. B* **57**, 1505 (1998).
  - <sup>44</sup> D. Sánchez-Portal, E. J. G. Santos, and A. Ayuela (2009), submitted.
  - <sup>45</sup> For simplicity and consistency we use throughout the paper the same nomenclature to label the different defect levels. However, it should be understood that for the noble metals and Zn the so-called antibonding  $A p_z-d_{z^2}$  level presents a sizeable contribution from the metal  $s$  orbital, while the degenerate  $E sp-d$  levels have non-negligible contributions from the  $p$  orbitals of the metal.
  - <sup>46</sup> R. Sielemann, Y. Kobayashi, Y. Yoshida, H. P. Gunnlaugsson, and G. Weyer, *Phys. Rev. Lett.* **101**, 137206 (2008).
  - <sup>47</sup> J. Barzola-Quicuía, R. Höhne, M. Rothermel, A. Setzer, P. Esquinazi, and V. Heera, *Eur. Phys. J B* **61**, 127 (2008).